ACS APPLIED ENERGY MATERIALS

www.acsaem.org Article

Modulating Charge Carrier Dynamics through Selective Surface Deposition of a CdS Layer to Boost the Performance of $AgBiS_2$ Q-Dot-Sensitized Solar Cells

Dimuthumal Rajakaruna, Hong-yi Tan, Chang-Feng Yan, and Jayasundera Bandara*

Cite This: https://doi.org/10.1021/acsaem.5c01968 Read Online

ACCESS | Metrics & More | Article Recommendations | Supporting Information

ABSTRACT: Despite having strong photoconductivity and a high absorption coefficient in Q-dot $AgBiS_2$, the efficiency of environmentally friendly light-harvesting $AgBiS_2$-based solar cells remains low at 10.0%, far below the theoretically estimated 20% efficiency with a current density of 22 mA/cm^2 and V_{oc} of 980 mV. The inherent short-carrier diffusion lengths and trap-assisted recombination properties of $AgBiS_2$ nanoparticles limit its thickness to ∼60 nm, beyond which a light parasite effect decreases performance. In this study, the charge carrier dynamics of the $AgBiS_2$ nanocrystalline film were modulated to minimize trap-assisted surface recombination and improve light harvesting by selective CdS layer coating in $AgBiS_2$ nanocrystals that resulted in an increase in J_{sc}, V_{oc}, and fill factor to 15.0 mA/cm^2, 0.352 V, and 47.0%, respectively, in contrast to $AgBiS_2$ without a CdS layer, which was 6.0 mA/cm^2, 0.248 V, and 37.0%. The electrochemical impedance data, IPCE measurements, and analysis of open-circuit voltage decay and intensity-dependent current/voltage parameters confirmed that the enhanced device performance was mostly due to a decrease in intrinsic trap-assisted recombination and the optical spacer effect. This study uniquely demonstrates the dual role of a selectively deposited CdS layer in $AgBiS_2$ nanocrystals, which inhibits trap-assisted recombination while also acting as a scattering layer.

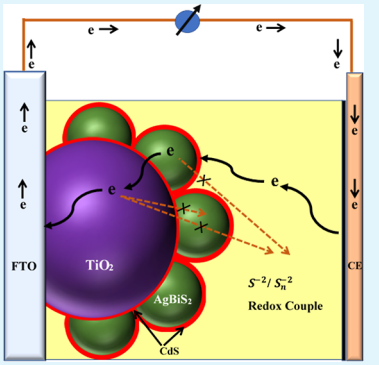

KEYWORDS: *$AgBiS_2$ photovoltaic, CdS, interface passivation, charge recombination, light scattering*

1. INTRODUCTION

Thin-film solar cells have emerged as a viable alternative to silicon-based photovoltaics due to their efficiency, stability, and most importantly, low production costs. Photovoltaic devices based on cadmium telluride (CdTe) and copper indium gallium selenide (CIGS) thin films have shown efficiencies of 18.6 and 20%, respectively.[1,2] Despite the accomplishment of reaching comparable efficiencies for CdTe and CIGS solar cells, concerns have been raised concerning production capacity limitations for CdTe and CIGS-based PV devices due to supply constraints in indium (In) and tellurium (Te). In terms of alternatives to CdTe and CIGS, ternary semiconductor materials would be next-generation photovoltaic materials. Among ternary semiconductor materials, antimony sulfide (Sb_2S_3) and silver bismuth sulfide ($AgBiS_2$) nanocrystal materials, which are readily available and nontoxic, are the most promising light-harvesters.[3,4]

Especially, $AgBiS_2$ quantum dots are a promising light-harvesting material for cost-effective photovoltaics due to their ideal bandgap, high absorption coefficient, environmental friendliness, broad absorption range, and excellent thermal stability, which is a critical factor for the stability of the device.[5−7] Recently, interest in $AgBiS_2$-based thin-film solar cells has increased, and as a result, considerable progress has been made in thin-film $AgBiS_2$ solar cells. Specifically, bigger-sized colloidal $AgBiS_2$ nanocrystals were used to achieve a PCE of 6.4%, resulting in smaller grain boundaries, greater mobility, and decreased trap-assisted recombination.[8] By the cation exchange process, Senina et al. were able to achieve a power conversion efficiency of 7.0% by obtaining highly monodispersed $AgBiS_2$ nanocrystals.[9] Similarly, stacking separate nanocrystalline $AgBiS_2$ with a potential gradient resulted in enhanced PCEs of 5.5−7.3% due to improved carrier movement helped by the potential gradient.[10−12] By ligand exchange approaches and cation disorder engineering, PCEs of 8.95−9.17% have been reported for $AgBiS_2$ Q-dot solar cells due to improved optical absorption properties of $AgBiS_2$ nanocrystals.[13] More recently, a remarkable efficiency of 10% for submicron-grain $AgBiS_2$ thin films synthesized via vapor-assisted solution process treatment has been reported by Li et al.[14] On the other hand, the progress of $AgBiS_2$ Q-dot sensitized solar cells, which are an alternative to thin-film solar cells, is not significant, reporting efficiencies of only 2.87 and 0.53% for solid hole conductors and polysulfide liquid

Received: July 2, 2025
Revised: August 29, 2025
Accepted: September 1, 2025

electrolyte, respectively.[15,16] Although the current efficiency of $AgBiS_2$ Q-dot sensitized solar cell is inferior to that of DSSC, the use of $AgBiS_2$ quantum dots as the light absorber allows for harvesting the full solar spectrum through fine control of the band gap, potentially leading to higher solar cell performance compared to DSSC.

The reported highest efficiency for thin-film $AgBiS_2$ Q-dots solar cells is 10%, delivering ~ 27 mA/cm^2, while for $AgBiS_2$ Q-dot sensitized solar cells, reported efficiencies are 2.87 and 0.53%, respectively, for solid hole-conductors and polysulfide liquid-electrolyte, delivering 13.2 and 7.6 mA/cm^2, respectively.[14,17,18] However, $AgBiS_2$, with a band gap energy of ~1.07 eV and an absorption coefficient of ~10^6 cm^{-1}, may reach a short-circuit current density (J_{sc}) of 22 mA/cm^2 and a conversion efficiency of 20.0% according to theoretical predictions.[19] In a recent study, a PCE of 26% has been estimated for $AgBiS_2$-based PV cells through theoretical study.[20,21] The difference between experimentally reported and theoretically expected J_{sc} and efficiency can be attributed to bulk and surface defects in $AgBiS_2$, leading to (a) inefficient charge collection properties of $AgBiS_2$ due to short-electron diffusion length and (b) the high-density trap states and energy cation disorder in $AgBiS_2$, which cause energy loss during charge carrier transport and collection.[13,22,23] Given the short charge diffusion lengths of electrons (60 nm) and holes (150 nm) in $AgBiS_2$ nanocrystals, a defect-free $AgBiS_2$ layer with a thickness of less than 60 nm is required for improved device performance, and beyond 60 nm $AgBiS_2$ layer thickness, a light parasite effect decreases the performance.[24] Several strategies have been employed to overcome energy loss in $AgBiS_2$-based solar cells, including the use of larger grain $AgBiS_2$,[25] cation disorder engineering,[13] solvent-engineering-assisted ligand exchange strategy,[26] mixed $AgBiS_2$ nanocrystals,[27] halide ion passivation of $AgBiS_2$ surface,[28] and nanowire heterojunction solar cells.[22]

Given the large specific interface area of $AgBiS_2$ nanocrystals, surface passivation is particularly beneficial for correcting surface imperfections. Surface passivation was discovered to be successful in producing thin $AgBiS_2$ nanocrystalline films free of surface morphological defects and with a low trap-state density, resulting in balanced charge carrier mobility and excellent charge transport across interfaces.[29,30] Passivating $AgBiS_2$ Q-dots with organic ligands as well as inorganic materials such as ZnS and MgO was found to reduce interface recombination and current leakage, resulting in significantly improved photovoltaic performance.[31−33] Although inorganic passivation is widely applied in Q-dot solar cells, the passivation of $AgBiS_2$ nanocrystals has received little attention. A CdS passivation layer, owing to its lattice compatibility with $AgBiS_2$, is hypothesized to suppress interfacial defects and recombination losses. In this study, the effect of CdS passivation on carrier dynamics and efficiency of $AgBiS_2$ Q-dot-sensitized solar cells is investigated.

However, little research has been undertaken on the passivation of $AgBiS_2$ Q-dot; therefore, in this study, an interface passivation by a CdS layer on the efficiency of $AgBiS_2$ Q-dot-sensitized solar cells was conducted to address the carrier losses in $AgBiS_2$ due to surface defects.

To address interfacial recombination losses in $AgBiS_2$ Q-dot solar cells, this study introduces a dual-interface passivation strategy in which thin CdS layers were selectively deposited both beneath and above the $AgBiS_2$ layer to passivate the electron-extracting ($AgBiS_2/TiO_2$) and hole-extracting ($AgBiS_2$/electrolyte) interfaces. This dual modification approach is more effective than conventional single-interface treatments in reducing charge carrier recombination. As a result, the overall charge separation and device performance are significantly improved. Additionally, it was noted that CdS is a better passivation material due to its broad light transmission and enhanced electron and hole mobilities. Furthermore, as the CdS layer also functions as a light-scattering layer, the light-parasite effect of $AgBiS_2$ can be reduced, and hence, this study underlined its dual role layer in improving the device performance of $AgBiS_2$ Q-dot sensitized solar cells.

2. EXPERIMENTAL SECTION

2.1. Preparation of Electron Transport Layer (ETL) and Deposition of $AgBiS_2$ Q-Dot. A TiO_2 paste, which was prepared by the modified Pichini method, was applied on the fluorine-doped tin oxide (FTO) glass to fabricate the mesoporous TiO_2 layer.[29,34] To prepare the TiO_2 paste, 1.33 mL of ethylene glycol was first heated to 60 °C, and 1.27 g of citric acid and 0.31 mL of titanium isopropoxide were added. The mixture was heated to 90 °C and kept there for 15 min to obtain a clear solution, followed by adding 0.56 g of P25 Degussa TiO_2 powder once the solution was cooled to room temperature. The prepared paste was ground for an hour to create a consistent paste, while the titanium isopropoxide: citric acid: ethylene glycol and titanium isopropoxide to TiO_2 powder molar ratios were kept at 1:6:24 and 1:7, respectively. Using the doctor blade technique, the resultant paste was applied on a previously cleaned FTO substrate having one layer of Scotch tape on it. The coated substrates were then sintered at 450 °C, with the temperature raised gradually at a rate of 3 °C per minute.

The Successive Ionic Layer Adsorption and Reaction (SILAR) technique was used to deposit $AgBiS_2$ quantum dots on the mesoporous TiO_2 layer.[34−36] In the preparation of $AgBiS_2$ layers, one SILAR cycle included several steps. First, the TiO_2 film on the FTO substrate was dipped for 30 s in an aqueous solution containing 0.017 M $AgNO_3$, followed by a rinse in deionized water for an additional 30 s. Next, the Ag^+-loaded electrode was immersed in a 0.025 M Na_2S solution for 30 s, accompanied by another rinse in deionized water for the same duration. The electrode was then dipped into a 0.025 M $Bi(NO_3)_3$ solution prepared in a mixture of distilled water and acetic acid for 30 s, followed by a rinse with deionized water of equal length. The process concluded with a second immersion in 0.025 M Na_2S for 30 s and a final 30 s rinse. To promote uniform film quality, air drying at room temperature was carried out after each immersion step. Once the deposition process was completed, the electrodes were stored overnight and then annealed at 100 °C for 1 h on a hot plate in ambient conditions.

2.2. Deposition of CdS Thin Layer. To examine the influence of passivation on device performance, a thin CdS layer was formed on either TiO_2 (TiO_2−CdS−$AgBiS_2$) or $AgBiS_2$ (TiO_2−$AgBiS_2$−CdS) using the SILAR process.[29] The FTO/TiO_2 substrate was immersed in a 0.05 M cadmium acetate ($Cd(Ac)_2$) solution for 1 min followed by washing with deionized water to deposit CdS on the TiO_2 substrate. The Cd^{2+}-impregnated FTO/TiO_2 electrode was immersed in 0.05 M Na_2S solution for 1 min and washed again, completing one SILAR cycle to create FTO/TiO_2/***CdS***. For the deposition of a CdS layer on $AgBiS_2$ (TiO_2−$AgBiS_2$−***CdS***), the same SILAR procedure was employed with the substrate FTO/TiO_2/$AgBiS_2$. On the other hand, for the deposition of CdS on both TiO_2 and $AgBiS_2$ (FTO/TiO_2−***CdS***/$AgBiS_2$−***CdS***), a stepwise deposition was carried out using the same SILAR approach.

2.3. Preparation of Polysulfide Electrolyte, Cu_2S-Coated Brass Counter Electrode, and Device Fabrication. The polysulfide electrolyte was made by dissolving 2 M Na_2S, 2 M S, and 0.2 M KCl in a 7:3 (v/v) mixture of methanol and water. To make a Cu_2S/brass counter electrode (CE), a brass plate was dipped in concentrated HCl at 90 °C and heated until HCl evaporated. The

https://doi.org/10.1021/acsaem.5c01968
ACS Appl. Energy Mater. XXXX, XXX, XXX−XXX

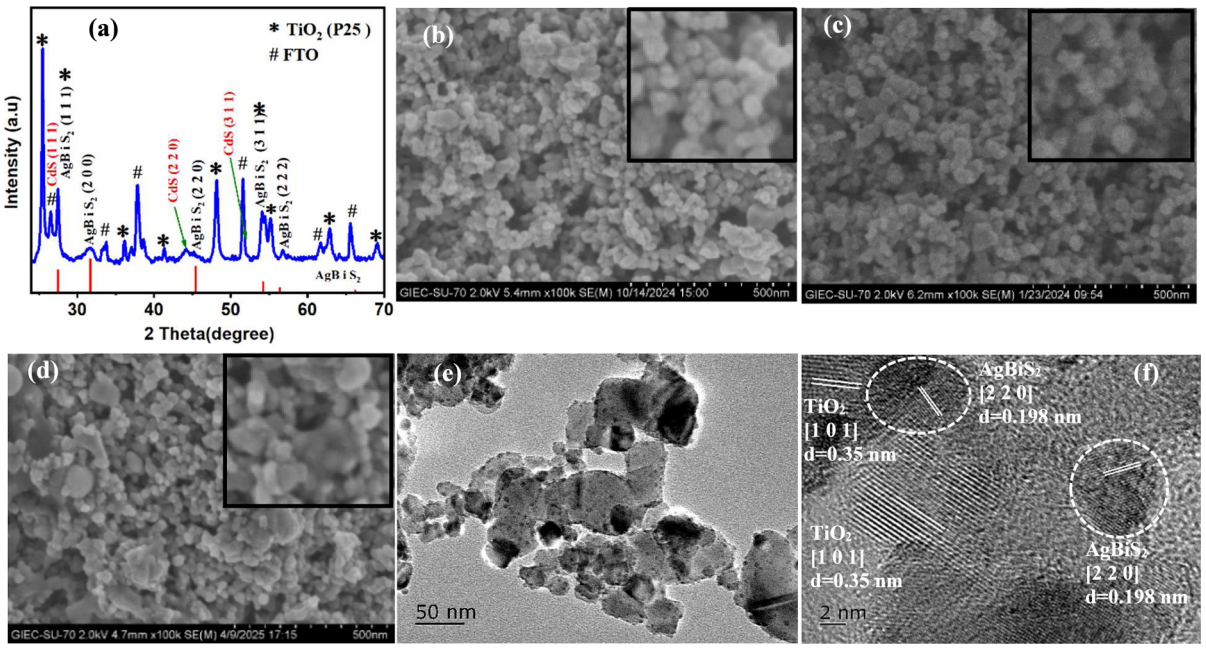

Figure 1. (a) XRD of FTO/m-TiO_2/$AgBiS_2$/**CdS**. Cross-sectional SEM images of (b) pristine TiO_2, (c) TiO_2/$AgBiS_2$, and (d) TiO_2/$AgBiS_2$/CdS. (e) LRTEM and (f) HRTEM images of TiO_2/$AgBiS_2$/CdS.

brass plate was then thoroughly cleaned with distilled water and dried. A hole-punched Parafilm spacer was placed on top of the cleaned brass plate (which had been treated with boiled HCl), and the produced polysulfide electrolyte was applied to the exposed part of the plate.[29,34] The solar cell was assembled by sandwiching the working electrode and the Cu_2S/Brass counter electrode with a binder clip and inserting the polysulfide electrolyte between the working electrode and the counter electrode. The active area of the testing instrument is 0.25 cm^2.

2.4. Characterization and Measurement Solar Cell Performance. A Thermal Field Emission Scanning Electron Microscope (S4800, Hitachi) was employed to examine the surface morphology of the films. Additionally, energy-dispersive spectroscopy (EDS) was utilized to analyze the elemental composition and distribution. A High-Resolution Field Emission Transmission Electron Microscope (JEM-2100F, NEC Corporation) was used to analyze the structural properties of the $AgBiS_2$ nanocrystals. To investigate the crystal structure of TiO_2, $AgBiS_2$, and CdS, X-ray Diffraction (XRD) analysis was conducted using a polycrystalline X-ray powder diffractometer (PANalytical X'Pert HighScore, X'Pert PRO MPD) with Cu Kα radiation. The surface composition of the as-synthesized samples was characterized by X-ray photoelectron spectroscopy (XPS) using a Thermo ESCALAB 250Xi multifunctional imaging electron spectrometer. The absorption spectra of the $AgBiS_2$ films, with FTO as a reference, were recorded using a Shimadzu UV−vis spectrophotometer (model 2450) over the wavelength range of 300 to 1100 nm. The current−voltage (I−V) characteristics of the solar cells were measured using a Zahner Zennium universal electrochemical workstation (measurement can be taken up to three decimal places) under one-sun illumination, provided by an AM1.5G solar simulator (Newport AAA, 100 mW/cm^2). All device measurements were repeated 10 times to ensure reproducibility. The results were consistent across these repetitions, confirming the reliability and consistency of the reported photocurrent, open-circuit voltage, and fill factor values. The dark I−V measurements were carried out by using a Zahner Zennium universal electrochemical workstation under dark conditions. External Quantum Efficiency (EQE) measurements were carried out as a function of wavelength (300−1100 nm) using a Bentham PVE300 photovoltaic characterization system. Open-circuit voltage decay (OCVD) measurements were conducted by using a RIGOL DS1054 digital oscilloscope. The device was illuminated until a stable voltage was reached, after which the light source was switched off, and the voltage decay was recorded over a specified time interval. Electrochemical impedance spectroscopy (EIS) was performed by using a Zahner Zennium universal electrochemical workstation equipped with a Thales frequency response analyzer. The measurements were carried out in the dark using a 10 mV AC signal over a frequency range of 0.1 Hz to 1 MHz. Mott−Schottky experiments were performed in a one-compartment three-electrode cell using the Zahner Zannium universal electrochemical workstation equipped with a frequency response analyzer (Thalas) at a 10 mV amplitude AC signal and at the frequency of 1 kHz in dark conditions with 0.5 M $Na_2SO_{4(aq)}$ electrolyte, a Pt counter electrode, and Ag/AgCl saturated KCl as the reference electrode.

3. RESULTS AND DISCUSSION

In this study, a CdS layer was selectively deposited on $AgBiS_2$ nanostructures to improve the performance of $AgBiS_2$ Q-dot-sensitized solar cells. Supporting Information provides a detailed investigation of the formation and surface morphologies of diverse nanostructures carried out by using XRD, SEM, and TEM analysis. According to XRD patterns in Figures 1a and S1, it was clear that the TiO_2 electron transport layer (ETL) on the FTO substrate is highly crystalline, containing both anatase and rutile phases.[37]

The deposition of light-harvesting $AgBiS_2$ nanocrystalline particles on the TiO_2 layer was confirmed by the presence of characteristic diffraction patterns of the cubic phase $AgBiS_2$ (Figure S1). The presence of CdS within the composite structure is important since it plays a dual role enhancing visible-light absorption (as a scattering layer) and as a passivation layer capable of reducing the surface recombination at the interfaces. The presence of peaks at 26.5°, 44.18°, and 52.06°, corresponding to the (111), (220), and (311) planes for CdS in Figure 1a, respectively, demonstrated successful CdS layer deposition in the TiO_2/$AgBiS_2$ electrode.

The presence of the CdS layer was confirmed by the cross-sectional SEM images and high-resolution TEM images shown in Figure 1. From the inspection of the cross-sectional images of TiO_2, TiO_2/$AgBiS_2$, and TiO_2/$AgBiS_2$/**CdS** shown in

https://doi.org/10.1021/acsaem.5c01968
ACS Appl. Energy Mater. XXXX, XXX, XXX−XXX

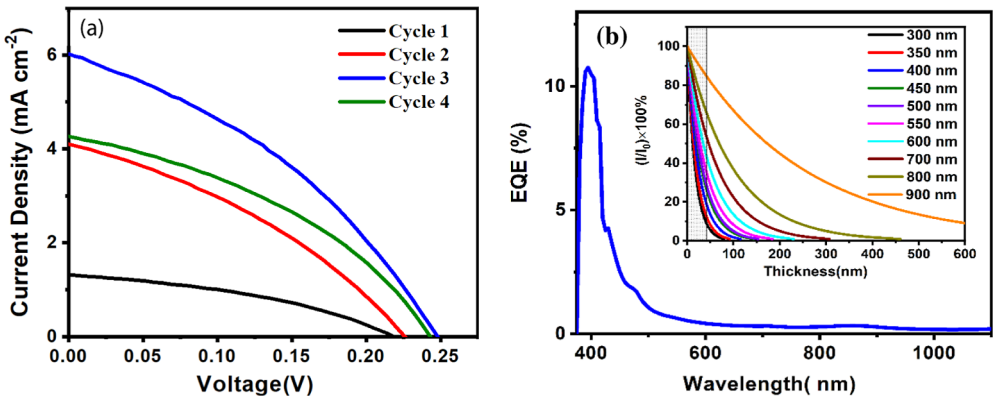

Figure 2. (a) Current density−voltage curves for FTO/TiO_2/$AgBiS_2$/polysulfide electrolyte/Cu_2S/brass with the variation of SILAR cycles and (b) EQE of the FTO/TiO_2/$AgBiS_2$/polysulfide electrolyte/Cu_2S/brass device for the optimized SILAR cycle. (inset) Wavelength-dependent light absorption proportion of $AgBiS_2$ as a function of layer thickness.

Figure 1b−d, respectively, it can be observed that the smooth TiO_2 surface (magnified image in inset in Figure 1b) becomes rough (magnified image in inset in Figure 1c) due to the presence of $AgBiS_2$ on the TiO_2 surface and a smear-like structure seen in Figure 1d, and the magnified inset in the same figure can be attributed to the CdS. Additionally, in the TEM image shown in Figure 1e, for TiO_2/$AgBiS_2$, the evenly distributed 7−10 nm particles visible on the surface of TiO_2 indicate that the surface was successfully decorated with $AgBiS_2$ nanoparticles, ensuring better coverage of $AgBiS_2$ Q-dots on the electron transport layer, which would result in enhanced light absorption properties. The corresponding *d*-spacing of 0.198 nm (Figure 1f) can be attributed to the (220) facet of $AgBiS_2$, in good agreement with the lattice planes characteristic for cubic-phase $AgBiS_2$, validating the observed nanodots as $AgBiS_2$ quantum dots. Since the CdS passivation layer formed via four SILAR cycles is extremely thin, it was not clearly resolved in TEM images; as such, the extent of its deposition is expressed in terms of the number of SILAR cycles rather than physical thickness. This approach is commonly adopted when direct imaging resolution is limited by the nanoscale dimensions of the deposited layers. Furthermore, Figure S2b illustrates Energy Dispersive X-ray Spectroscopy (EDS) mapping of the cross-section picture in Figure 1d, exhibiting even distribution of Ti, Ag, Bi, S, and Cd, showing homogeneous incorporation of $AgBiS_2$ and CdS. On the other hand, EDS mapping of the TEM image of Figure 1e further reveals that the dot-like structures contain Ag, Bi, Cd, and S elements, explaining the coexistence of $AgBiS_2$ and CdS at the nanoscale (Figure S3). Structural characterizations shown in Figures 1, S1, and S2 (XRD, SEM, EDS, and TEM) confirm the formation of well-crystallized, uniformly distributed $AgBiS_2$ nanocrystals with controlled CdS coverage. This morphology facilitates efficient charge transport by minimizing grain boundaries and reducing trap states. The improved crystallinity and surface coverage correlate with the observed enhancements in the photocurrent and reduced recombination. To investigate the effect of selective surface deposition of a thin CdS on the device performance and charge carrier dynamics of $AgBiS_2$ Q-dot sensitized solar cells, the device performance of TiO_2/***CdS***/$AgBiS_2$, TiO_2/$AgBiS_2$/*CdS*, and TiO_2/***CdS***/$AgBiS_2$/***CdS*** electrodes was evaluated.

As the first step, the thickness of the $AgBiS_2$ layer was tuned, and the influence of CdS on charge carrier dynamics was investigated for the optimized $AgBiS_2$ thickness. Figure 2a and Table 1 show that the highest efficiency was attained when the $AgBiS_2$ layer thickness was 40 nm $AgBiS_2$, and as the $AgBiS_2$ layer thickness increased beyond 40 nm, the efficiency decreased drastically. The thickness of $AgBiS_2$ thin films was estimated from UV−Visible absorbance data using the relation $A(\lambda) = \alpha(\lambda)\cdot d$, where $A(\lambda)$ is the absorbance at a specific wavelength, $\alpha(\lambda)$ is the absorption coefficient, and d is the film thickness.[38] (For further details refer to Figure S4 and the related text). On the other hand, beyond 40 nm thick, J_{sc} decreases while V_{oc} remains the same, indicating that the device performance is significantly dependent on J_{sc} compared to V_{oc}, which in turn is highly dependent on the light harvesting efficiency and the thickness of $AgBiS_2$ film. The optimum $AgBiS_2$ layer thickness can be explained considering the light absorption coefficients and the electron diffusion length of $AgBiS_2$, and the IPCE response of the $AgBiS_2$ electrode.

Table 1. Solar Cell Parameters and Absorbance Thickness with Changing Number of SILAR Cycles

no of SILAR cycle	V_{oc} (V)	J_{sc} (mA cm^{-2})	FF (%)	η (%)
1	0.218	1.3	38.5	0.11
2	0.225	4.1	34.7	0.32
3	0.248	6.0	37.0	0.55
4	0.244	4.2	39.0	0.40

As shown in Figure 2b, the EQE response of the 40 nm thick $AgBiS_2$ of the TiO_2/$AgBiS_2$ electrode is primarily observed up to 500 nm, with a very weak response observed in the 600−1000 nm region, which can be attributed to both the poor light-harvesting efficiency and charge collection efficiency. The inset in Figure 2b shows that an optimum $AgBiS_2$ thickness of 40 nm can absorb 90% of incoming 300−400 nm photons which was estimated using the Beer−Lambert law $I(x) = I_0\, e^{-ax}$, in which the I_0 is the incident photon flux and the $I(x)$ is the photon flux in $AgBiS_2$ and taking the corresponding absorption coefficients α of $AgBiS_2$ at different wavelengths.[39] However, with the same $AgBiS_2$ thickness, only 70−35% of photons are absorbed in the 500−800 nm region, requiring a thickness greater than 100 nm for efficient capture of 500−1000 nm photons. However, as the electron diffusion length of $AgBiS_2$ is restricted to ∼60 nm,[40] the excited charge carriers generated outside the 50−60 nm $AgBiS_2$ layer thickness cannot be collected efficiently due to higher charge recombination,

https://doi.org/10.1021/acsaem.5c01968
ACS Appl. Energy Mater. XXXX, XXX, XXX−XXX

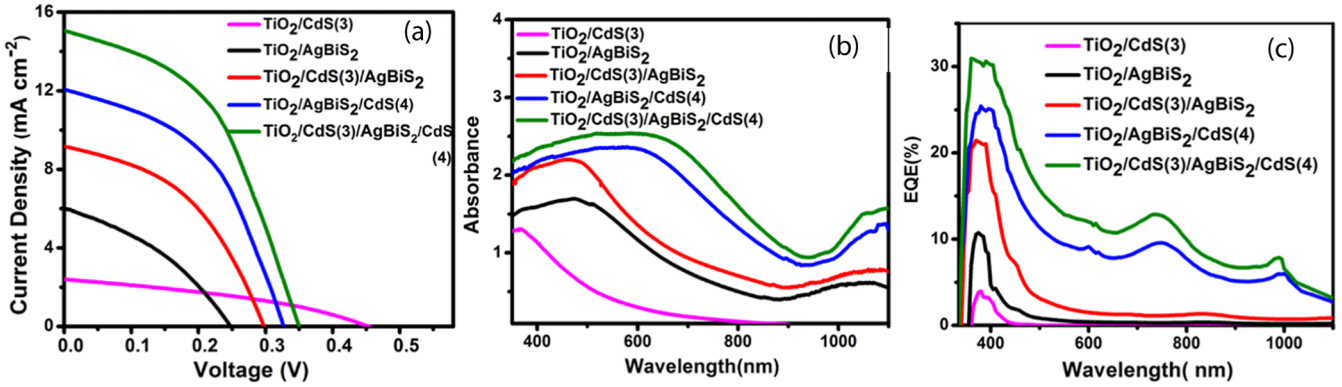

Figure 3. (a) Current density−voltage curves, (b) UV−visible spectra, and (c) EQE curves for FTO/TiO_2/***CdS(3)***, FTO/TiO_2/$AgBiS_2$, FTO/TiO_2/***CdS(3)***/$AgBiS_2$, FTO/TiO_2/$AgBiS_2$/***CdS(4)***, and FTO/TiO_2/***CdS*** (3)/$AgBiS_2$/***CdS(4)*** cell configurations.

Table 2. Solar Cell Parameters of TiO_2/*CdS*, TiO_2/$AgBiS_2$, TiO_2/(*CdS*(3))/$AgBiS_2$, TiO_2/$AgBiS_2$/(*CdS*(4)), and TiO_2/*CdS*(3)/$AgBiS_2$/*CdS*(4)/Polysulfide Electrolyte/Cu_2S Interfaces

	V_{oc} (V)	J_{sc} (mA cm^{-2})	FF (%)	η (%)
TiO_2/CdS(3)	0.452	2.4	36.9	0.40
TiO_2/$AgBiS_2$	0.248	6.0	37.0	0.55
TiO_2/CdS(3)/$AgBiS_2$	0.297	9.2	44.3	1.20
TiO_2/$AgBiS_2$/CdS(4)	0.327	12.1	45.5	1.80
TiO_2/CdS(3)/$AgBiS_2$/CdS(4)	0.352	15.0	47.0	2.46

and hence, the weak IPCE response in the 500−1000 nm region can be justified. Hence, the balance between charge carrier diffusion length and the light absorption coefficients of $AgBiS_2$ resulted in a maximum thickness of ∼40 nm. The absorption coefficient (α) and electron diffusion length values presented in this study were extracted from previously reported data on $AgBiS_2$ quantum dot systems and are used here for preliminary estimation purposes.[39,40]

To investigate the effect of selective surface deposition of a thin CdS on the device performance and charge carrier dynamics, the $AgBiS_2$ layer thickness was kept at ∼40 nm, and device performance was investigated by varying the CdS layer thicknesses on the TiO_2 surface (TiO_2/***CdS***/$AgBiS_2$), the $AgBiS_2$ surface (TiO_2/$AgBiS_2$/*CdS*), or both the TiO_2 and $AgBiS_2$ surfaces (TiO_2/***CdS***/$AgBiS_2$/***CdS***). As shown in Figure S5a,d, the optimum CdS layer thicknesses for TiO_2/***CdS***/$AgBiS_2$ and TiO_2/$AgBiS_2$/*CdS* device structures are three and four SILAR cycles, respectively. Hence, the IV results, absorption spectra, and EQE response for TiO_2/***CdS(3)***/$AgBiS_2$, TiO_2/$AgBiS_2$/***CdS(4)***, and TiO_2/***CdS(3)***/$AgBiS_2$/***CdS(4)*** electrode structures with the $AgBiS_2$ thickness of 40 nm are shown in Figure 3a−c, respectively, while the current density (J_{sc}), open-circuit voltage (V_{oc}), FF, and efficiency (η) are given in Table 2. For comparison, the solar cell parameters of TiO_2/$AgBiS_2$ and TiO_2/***CdS*** are also shown in Table 2.

For TiO_2/$AgBiS_2$ and TiO_2/***CdS*** device structures, the observed solar cell efficiencies are 0.55 and 0.40, having J_{sc} of 6.0 and 2.4, respectively. However, the solar cell performance shown in Figure 3a indicates that the presence of an optimum thin CdS layer in between TiO_2−$AgBiS_2$ (TiO_2−**CdS**−$AgBiS_2$), over the $AgBiS_2$ (TiO_2−$AgBiS_2$−**CdS**) and on both TiO_2 and $AgBiS_2$ (TiO_2−**CdS**−$AgBS_2$−**CdS**), resulted in overall efficiency enhancement of ∼2.2, 3.2, and 4.5 times compared to without a CdS layer (TiO_2−$AgBiS_2$). Furthermore, the increase in J_{sc} of the individual electrodes found to be ∼1.5, 2.0, and 2.5 times as compared to the electrode without the CdS layer. Significant factor noted from these IV results was that the coating of CdS on $AgBiS_2$ (i.e TiO_2/$AgBiS_2$/***CdS***(4)) is more significantly contributes to the enhanced device performance compared its presence on TiO_2 (i.e TiO_2/***CdS***(3)/$AgBiS_2$), whereas presence of CdS layer on both TiO_2 and $AgBiS_2$ (i.e TiO_2/***CdS***(3)/$AgBiS_2$/***CdS***(4)) yielded the highest performance, indicating the importance of selective deposition of the passivation layer for the enhancement of device performance. Furthermore, the EQE response is greatly enhanced after coating of CdS on $AgBiS_2$ and the variations of EQE responses shown in Figure 3c is highly correlated to the absorption pattern variation of $AgBiS_2$ rather than CdS shown in Figure 3b.

To better understand the role of CdS, Figure 3b,c shows the absorption and EQE response of TiO_2/***CdS***, TiO_2/$AgBiS_2$, TiO_2/***CdS***(3)/$AgBiS_2$, TiO_2/$AgBiS_2$/***CdS***(4), and TiO_2/***CdS***(3)/$AgBiS_2$/***CdS***(4), respectively, while Figure S5b,e,c,f depicts the variation in absorption and EQE response with CdS layer thicknesses. As shown in Figure 3b, CdS absorbs mainly in the 300−500 nm region with an absorption threshold of ∼500 nm, while $AgBiS_2$ absorbs in the 300−1100 nm region, extending its absorption to the IR region. As shown in Figure S6, the Tauc plots of TiO_2/$AgBiS_2$, TiO_2/CdS(3)/$AgBiS_2$, TiO_2/$AgBiS_2$/CdS(4), and TiO_2/CdS(3)/$AgBiS_2$/CdS(4) showed that the optical band gap decreased from 1.90 eV for (**TiO_2/$AgBiS_2$**) to 1.44 eV for (TiO_2/**CdS(3)**/$AgBiS_2$/**CdS(4)**) with the introduction of CdS layers. Adding a CdS layer at the bottom (TiO_2/CdS(3)/$AgBiS_2$) lowered the band gap to 1.87 eV, whereas a top CdS layer (TiO_2/$AgBiS_2$/CdS(4)) resulted in a larger shift to 1.48 eV. The dual-passivated structure had the smallest band gap of 1.44 eV, demonstrating that CdS layers significantly improve visible light absorption and interfacial characteristics by eliminating surface defects and changing band alignment. As shown in Figure 3c, the EQE response of TiO_2/CdS is limited to the 300−500 nm range and strongly correlated to the

https://doi.org/10.1021/acsaem.5c01968
ACS Appl. Energy Mater. XXXX, XXX, XXX−XXX

absorption pattern of CdS. In the case of $TiO_2/AgBiS_2$, despite a strong absorption in 300−1100 nm, the EQE response is very poor, implying that the photoexcited charge carriers in $AgBiS_2$ are not effectively collected. Interestingly, after coating a thin CdS layer on $AgBiS_2$ nanoparticles (i.e., the device $TiO_2/AgBiS_2/$***CdS***), as depicted in Figure 3c, the EQE response is dramatically enhanced in the 300 to 1100 nm region, and its response strongly corresponds to the absorption pattern of $AgBiS_2$ shown in Figure 3b, indicating that it acts as a passivation layer on $AgBiS_2$. A close examination of the EQE spectra reveals that the introduction of CdS deposition cycles alters the spectral shape and significantly increases the quantum efficiency in the long-wavelength region, implying that it acts not only as a passivation layer but also as a scattering layer, facilitating $AgBiS_2$ light harvesting. However, a coating of a CdS layer on TiO_2 of the device structure $TiO_2/$***CdS***$/AgBiS_2$, despite having a strong absorption due to $AgBiS_2$ (Figure 3b), the enhancement in EQE response (Figure 3c) is mainly observed in the 300−500 nm, revealing that the CdS layer contributes mainly to TiO_2 passivation and does not significantly passivate the $AgBiS_2$ quantum dots. These results demonstrate the importance of properly placing the CdS layer on $AgBiS_2$ for better charge generation as well as collection, and hence, as shown in Figure 3, the presence of a CdS layer on $AgBiS_2$ ($TiO_2/AgBiS_2/$***CdS***), and on both $TiO_2/AgBiS_2$ ($TiO_2/$***CdS***$(3)/AgBiS_2/$***CdS***(4)), the EQE response is enhanced and well distributed in the 300−1100 nm corresponding to the absorption pattern of $AgBiS_2$, delivering J_{sc} of 12.1 and 15.0 mA/cm^2, respectively, due to significant contribution from $AgBiS_2$. Furthermore, the EQE-integrated current density curve shown in Figure S5g confirms the current density values listed in Table 2.

It should be mentioned that the increase in absorption after CdS coating on $TiO_2/AgBiS_2/CdS$ (Figure 3b) is caused by the saturation of dangling S atoms of the $AgBiS_2$ by the extra sulfur source during the deposition. As shown in Figure S7a, the original $AgBiS_2$ color changed from dark brown to light brown during the annealing process, resulting in a slight decrease in absorption, whereas during the CdS deposition step, as it was dipped again in a sulfur source, the color changed back to dark brown (black) with increased absorption. However, the IV data shown in Figure S7b for the dark-brown (black) $TiO_2/AgBiS_2$ electrode has nearly the same IV performance, confirming that the additional contribution to the device performance is minimal due to that enhanced absorption, and thus performance improvement following the CdS coating on $AgBiS_2$ cannot be attributed to the light-harvesting characteristics of $AgBiS_2$. Furthermore, the Mott−Schottky analysis of $AgBiS_2$ shown in Figure 4 and Table 3 indicates that the flat band (FB) potential of $AgBiS_2$ is not changed due to CdS coating, implying that the observed enhanced solar cell efficiency is not attributable to enhanced charge transfer from the excited $AgBiS_2$ to the TiO_2 ETL. The observed increase in charge carrier density following CdS coating on $AgBiS_2$ could be attributed to $AgBiS_2$ passivation, which may give improved electron transport characteristics and lead to an increased charge collection. As proof of surface passivation of $AgBiS_2$ by CdS (i.e. chemical interaction between CdS and $AgBiS_2$), the XPS spectra of $AgBiS_2$ before and after CdS passivation are shown in Figure S8. When the core-level spectra of Ag 3d, Bi 4f, and S 2p of $AgBiS_2/CdS$ were compared to pristine $AgBiS_2$, notable binding energy shifts for the CdS-coated $AgBiS_2$ support the idea that the local

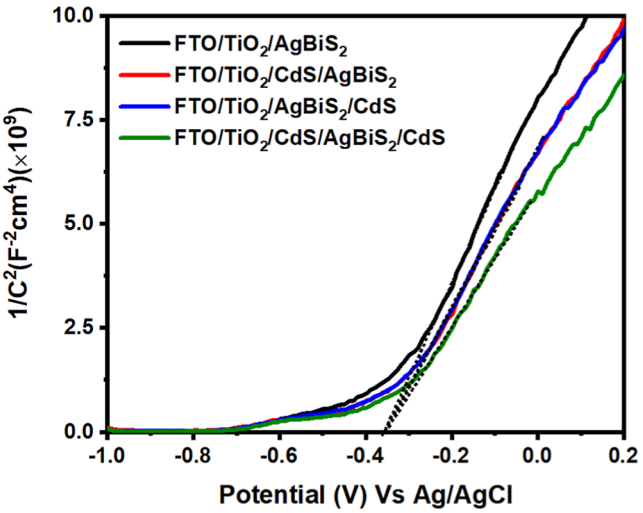

Figure 4. Mott−Schottky plots of the $TiO_2/AgBiS_2$, $TiO_2/$(***CdS(3)***)$/AgBiS_2$, $TiO_2/AgBiS_2/$(***CdS(4)***), and $TiO_2/$*CdS(3)*$/AgBiS_2/$***CdS(4)*** electrodes.

Table 3. FB Potential and Charge Carrier Density of the $TiO_2/AgBiS_2$, $TiO_2/$(CdS(3))$/AgBiS_2$, $TiO_2/AgBiS_2/$(CdS(4)), and $TiO_2/CdS(3)/AgBiS_2/CdS(4)$ Electrode

cell configuration	flat band potential (V) vs Ag/AgCl	charge carrier density ($\times 10^{16}$ m^{-3})
$TiO_2/AgBiS_2$	−0.357	6.57
$TiO_2/CdS(3)/AgBiS_2$	−0.351	7.89
$TiO_2/AgBiS_2/CdS(4)$	−0.350	7.97
$TiO_2/CdS(3)/AgBiS_2/CdS(4)$	−0.349	9.35

structure and electronic environment were altered beyond the $AgBiS_2$ and CdS interface bonding (for more information, see Figure S8 and the associated explanation in SI). The substantial peak shift for S 2p indicated interface charge transfer, most likely owing to surface sulfur vacancy passivation or Cd−S bond formation. Hence the negative binding energy shifts in Ag 3d (Figure S8a), Bi 4f, and S 2p (Figure S8b), indicating successful surface passivation and reduced defect density.

As demonstrated, the solar cell efficiency improves in the order ($TiO_2/AgBiS_2$) < ($TiO_2/$***CdS***$/AgBiS_2$) < ($TiO_2/AgBiS_2/$***CdS***) < ($TiO_2/$***CdS***$/AgBiS_2/$*CdS*) for different device structures with the same $AgBiS_2$ thickness, and a closely related EQE-absorption response was observed only when CdS was present on $AgBiS_2$. In all of these cases, the increase in J_{sc} was observed while keeping the $AgBiS_2$ layer thickness constant, indicating that the observed higher J_{sc} is not due to an increase in light absorption by $AgBiS_2$ or a CdS layer, as evidenced by the light absorption spectra and EQE measurements. However, a close look at the EQE spectra revealed the significant enhancement of the quantum efficiency in the long-wavelength region after CdS deposition on $AgBiS_2$, suggesting that CdS is acting not only as a passivation layer but also as a scattering layer facilitating the light harvesting of $AgBiS_2$ (See Figure S4 and Supporting Information).

The different role played by the CdS layer in the $TiO_2/AgBiS_2/$***CdS*** electrode could be that it can function as a passivation layer in minimizing the surface defects in $AgBiS_2$ while it could function as a light scattering layer too. Interestingly, *I*−*V* results show that the overall efficiency

https://doi.org/10.1021/acsaem.5c01968
ACS Appl. Energy Mater. XXXX, XXX, XXX−XXX

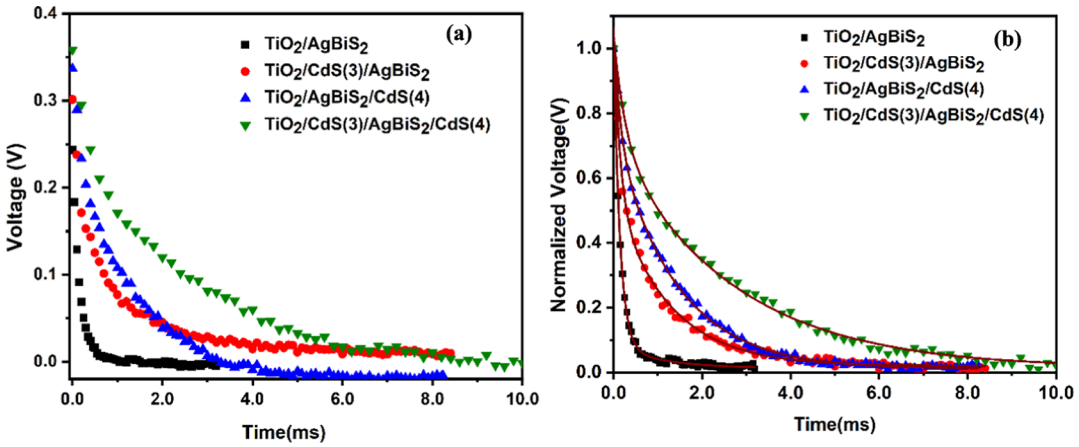

Figure 5. (a) OCVD curves and (b) fitted normalized OCVD curves for cell configurations: $TiO_2/AgBiS_2$, $TiO_2/(\boldsymbol{CdS(3)})/AgBiS_2$, $TiO_2/AgBiS_2/(\boldsymbol{CdS(4)})$, and $TiO_2/(\boldsymbol{CdS(3)})/AgBiS_2/(\boldsymbol{CdS(4)})$.

Table 4. Fitted Results for Open-Circuit Voltage Decay (OCVD) Curves

cell configuration	$A_1(A_1/(A_1 + A_2))$	τ_1 (μs)	$A_2(A_2/(A_1 + A_2))$	τ_2 (ms)
$TiO_2/AgBiS_2$/electrolyte	0.8512(84.7%)	138.1	0.1534(15.3%)	0.99
$TiO_2/\boldsymbol{CdS}(3)/AgBiS_2$/electrolyte	0.5212(49.8%)	141.7	0.5242(50.2%)	1.24
$TiO_2/AgBiS_2/\boldsymbol{CdS}(4)$/electrolyte	0.3012(29.2%)	151.8	0.7299(70.8%)	1.39
$TiO_2/\boldsymbol{CdS}(3)/AgBiS_2/\boldsymbol{CdS}(4)$/electrolyte	0.3229(31.4%)	272.9	0.7033(68.6%)	2.69

improvement is strongly correlated with an increase in J_{sc} values, implying that photoexcited charge carriers are efficiently collected and charge recombination is significantly reduced, which could be attributed to passivation of $AgBiS_2$ caused by the CdS coating. As demonstrated below, the estimated lifetime (τ) by the photovoltage decay measurements and the interfacial charge carrier dynamics investigation by electrochemical impedance spectroscopy measurements of $TiO_2/AgBiS_2/\boldsymbol{CdS}$ photoanodes with varied designs strongly evidence that the CdS serves as a surface passivation layer for defects-rich $AgBiS_2$ nanocrystals.

The open-circuit voltage decay (OCVD) measurements over time were carried out to investigate carrier recombination dynamics in each of the four cell configurations, which is an important tool to analyze the recombination behavior at the Q-dot electrolyte interface. The OCVD curves of cell configurations, $TiO_2/AgBiS_2$, $TiO_2/(\boldsymbol{CdS(3)})/AgBiS_2$, $TiO_2/AgBiS_2/(\boldsymbol{CdS(4)})$, and $TiO_2/(\boldsymbol{CdS(3)})/AgBiS_2/(\boldsymbol{CdS(4)})$ are shown in Figure 5a, whereas Figure 5b shows the normalized fitted results for the same electrodes. The OCVD results revealed a fast voltage decay pattern for the TiO_2−$AgBiS_2$, and once a CdS layer is coated on the TiO_2 layer of the $TiO_2/(\boldsymbol{CdS(3)})/AgBiS_2$ electrode, a noticeably slower voltage decay was observed, whereas its presence on the $AgBiS_2$ layer of the $TiO_2/AgBiS_2/(\boldsymbol{CdS(4)})$ electrode significantly slowed voltage decay, indicating that the major charge recombination occurs via the Q-dot $AgBiS_2$ particle. The minimum voltage decay rate was noted for the electrodes in which both TiO_2 and $AgBiS_2$ were passivated with a CdS layer.

In OCVD measurements, the lifetime of electrons (τ) can be estimated, as τ is related to the OCVD rates, as given in eq 1, in which K_B is the Boltzmann constant (1.38×10^{-23} J K^{-1}), T is the temperature, q is the elementary charge (1.69×10^{-19} C), and dV_{oc}/dt is the derivative of the open circuit voltage transient, and assuming that the electron recombination is linear with a first-order dependence on electron concentration and that it only occurs with the electrolyte.[41−43]

$$\tau = \left(\frac{K_B T}{q}\right)\left(\frac{dV_{oc}}{dt}\right)^{-1} \quad (1)$$

The nonlinear nature and exponential decay of the OCVD curves, as shown in Figure 5a, prevent them from being successfully fitted to an exponential decay pattern. However, the nonlinear behavior of the OCVD curves can be successfully explained by the exponential fit of OCVD curves given in eq 2 where V_0 is the open circuit voltage at the termination of excitation.[44,45]

$$V_{oc}(t) = \frac{kT}{q}\left[\exp\left(\frac{qV_0}{K_B T} - 1\right)\right]\exp\left(\frac{-t}{\tau}\right) \quad (2)$$

Equation 2, however, is unable to fit the OCVD data in Figure 5a for a single nonlinear exponential decay because the OCVD decay curves indicate that electron recombination is a multistep process that involves strong trap-assisted recombination, with a progressive decay process after a very rapid decay process in the initial stage. Therefore, in accordance with eq 3, the voltage decay curves were fitted with a two exponential decay process, and the fitted results are shown in Table 4 and Figure 5b.[46,47]

$$V = A_1\exp\left(-\frac{t}{\tau_1}\right) + A_2\exp\left(-\frac{t}{\tau_2}\right) + V_0 \quad (3)$$

By fitting the decay curves to a biexponential decay pattern, the fast-decaying term (τ_1) resulting from intrinsic trapping-assisted recombination in $AgBiS_2$ and the slow-decaying term (τ_2) resulting from interfacial recombination at the $AgBiS_2$-electrolyte and $AgBiS_2$−TiO_2 interfaces were extracted and presented in Table 4. The observed τ_1 values, especially for nonpassivated $TiO_2/AgBiS_2$ and passivated $TiO_2/AgBiS_2/$

https://doi.org/10.1021/acsaem.5c01968
ACS Appl. Energy Mater. XXXX, XXX, XXX−XXX

(*CdS*), are 138.1 and 151.8 μs, respectively, which differ less significantly between nonpassivated and passivated $AgBiS_2$, owing to the recombination by the intrinsic trapping-assisted recombination in $AgBiS_2$, which is an inherent property of the material. However, it was noted that the enhancement of τ_1 in the presence of CdS on both TiO_2 and $AgBiS_2$ (TiO_2/(*CdS(3)*)/$AgBiS_2$/(*CdS(4)*)) and the increase in τ_1 compared to that of TiO_2/$AgBiS_2$/(*CdS*) is likely due to the saturation of dangling S atoms of $AgBiS_2$ by extra sulfur source during the deposition, resulting in lower trap states in $AgBiS_2$. Although CdS passivation of $AgBiS_2$ has less effect on bulk recombination, it can significantly reduce interfacial recombination at the $AgBiS_2$-electrolyte and $AgBiS_2$−TiO_2 interfaces. Hence, the decrease in interfacial recombination at the $AgBiS_2$-electrolyte and $AgBiS_2$−TiO_2 interfaces due to passivation by CdS results in a considerable rise in τ_2 values from 0.99 to 1.39 ms for passivated $AgBiS_2$. On the other hand, the double passivated TiO_2/(*CdS(3)*)/$AgBiS_2$/(*CdS(4)*) design had the highest τ_2 value of 2.69 ms, which indicates a significant reduction in interfacial recombination at the $AgBiS_2$-electrolyte and $AgBiS_2$−TiO_2 interfaces, which is supported by the observed highest efficiency for the same design. It should be mentioned that the observed differences in τ_1 and τ_2 compared to previously reported values are primarily due to a change in the electrolyte composition (methanol/water mixture with a ratio of 4:1 was used) used in the OCVD measurements in this study, which alters the redox dynamics and interfacial recombination behavior at the $AgBiS_2$/electrolyte interface, resulting in changes in charge carrier lifetimes, which is reflected in the new fitted τ_1 and τ_2 values.[34] However, the variation and the behavior of τ_1 and τ_2 values of nonpassivated TiO_2/$AgBiS_2$ and passivated TiO_2/$AgBiS_2$/(*CdS*) are consistent within our systems and measurement conditions of this study and the previous study.

The τ_1 and τ_2 values of OCVD fitting data clearly demonstrated a reduction in recombination losses at the $AgBiS_2$-electrolyte after passivation. The variation in the parameters A_1 and A_2 in eq 3 determines the amplitude of trap-assisted recombination and interfacial recombination, respectively, and as given in Table 4, A_1 and A_2 factors are 84.7 and 15.3%, respectively, for the nonpassivated structure, indicating that charge loss is mainly due to intrinsic trapping-assisted recombination loss. After passivation, A_1 has declined to 29.2% and A_2 has increased to 70.8%, showing that the trap-assisted charge recombination path has been greatly reduced and that the charge loss is predominantly due to interfacial recombination at the $AgBiS_2$ electrolyte. Overall, the results of the OCVD indicate that the CdS layers successfully minimize the fast and slow charge recombination processes. Furthermore, despite the relative weight of A_2 being increased from 15.3% to 70.8%, the time constant τ_2 was also increased significantly after CdS passivation, leading to the reduced interfacial recombination at $AgBiS_2$ electrolyte and $AgBiS_2$−TiO_2, thereby increasing charge collection efficiency and solar cell efficiency.

Impedance spectroscopic studies were also performed to explore the interfacial charge dynamics of passivated and nonpassivated Q-dot $AgBiS_2$ electrodes, which provides information especially about electron lifetime and charge recombination at both anodes and cathodes. A Nyquist plot obtained for electrodes TiO_2/$AgBiS_2$, TiO_2/(*CdS(3)*)/$AgBiS_2$, TiO_2/$AgBiS_2$/(*CdS(4)*), and TiO_2/(*CdS(3)*)/$AgBiS_2$/(*CdS(4)*) is shown in Figure 6. The collected impedance data are fitted into two RC circuits connected in series to another series resistance, and the equivalent circuit employed to evaluate the impedance data is shown in an inset in Figure 6, and resistance values R_s (series resistance), R_{ct} (charge transport resistance), and R_{cr} (charge recombination resistance) for passivated and nonpassivated electrodes are given in Table 5.

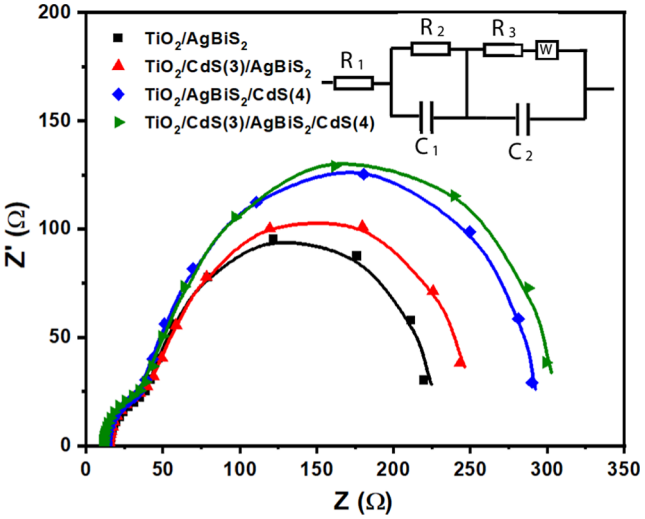

Figure 6. Electrochemical impedance spectroscopy (EIS) curves of TiO_2/$AgBiS_2$, TiO_2/(*CdS(3)*)/$AgBiS_2$, TiO_2/$AgBiS_2$/(*CdS(4)*), and TiO_2/(*CdS(3)*)/$AgBiS_2$/(*CdS(4)*), and the inset shown is the equivalent circuit used for fitting of EIS data.

Table 5. Fitted Results for Electrochemical Impedance Spectroscopy (EIS) Curves

cell configuration	R_0 (Ω)	R_{ct} (Ω)	R_{CR} (Ω)
TiO_2/$AgBiS_2$	15.4	21.7	86.4
TiO_2/CdS(3)/$AgBiS_2$	14.5	25.2	87.5
TiO_2/$AgBiS_2$/CdS(4)	12.6	22.8	107.1
TiO_2/CdS(3)/$AgBiS_2$/CdS(4)	13.87	33.78	138.5

As shown in Figure 6, for the electrode design TiO_2/$AgBiS_2$ without a CdS passivation layer with R_s, R_{ct}, and R_{CR} values of 15.4, 21.7, and 86.4 Ω, respectively, implies considerable recombination losses. By introducing a CdS layer on TiO_2 (TiO_2/(*CdS(3)*)/$AgBiS_2$), a marginal increase in R_{ct} and R_{CR} to 25.2 and 87.5 Ω was noted, indicating that the trap-assisted or interfacial recombination does not play a significant role in minimizing the interfacial charge recombination. However, R_{CR} is increased to 107.1 Ω after coating of a thin CdS layer on the $AgBiS_2$ (i.e., TiO_2/$AgBiS_2$/(*CdS(4)*)), indicating that the passivation on the $AgBiS_2$ surface is more effective in suppressing interfacial charge recombination. Furthermore, the increase in the R_{CR} from 87.5 to 138.5 Ω after passivation of both TiO_2 and $AgBiS_2$ confirms that the growth of CdS layers leads to a significant reduction in the recombination rates. Overall, EIS analysis found that CdS passivation on the $AgBiS_2$ surface effectively inhibits charge recombination. Passivation on both TiO_2 and $AgBiS_2$ significantly increased recombination resistance, suggesting enhanced charge carrier dynamics at the $AgBiS_2$/CdS interface compared to the bare $AgBiS_2$.

To further confirm the decrease in the trap-assisted charge recombination by the passivation of defects in $AgBiS_2$ by coating a CdS layer on $AgBiS_2$, light intensity-dependent

https://doi.org/10.1021/acsaem.5c01968
ACS Appl. Energy Mater. XXXX, XXX, XXX−XXX

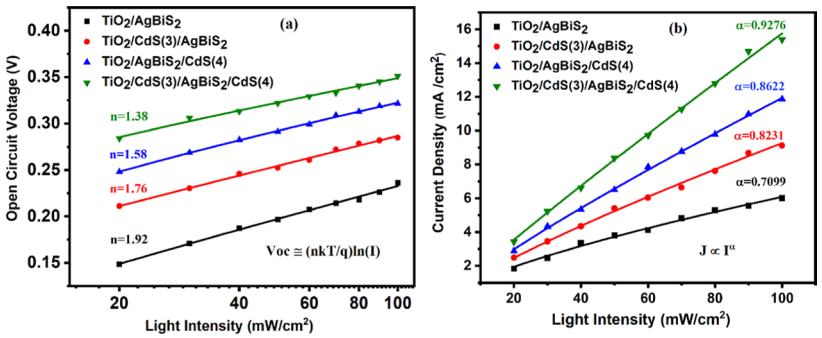

Figure 7. Light intensity-dependent measurements of voltage and current density; (a) V_{oc} versus light intensity and (b) J_{sc} versus light intensity curves for $TiO_2/AgBiS_2$, $TiO_2/(CdS(3))/AgBiS_2$, $TiO_2/AgBiS_2/(CdS(4))$, and $TiO_2/(CdS(3))/AgBiS_2/(CdS(4))$.

measurements of open-circuit voltage (V_{oc}) and current density (J_{sc}) were conducted, as shown in Figure 7a,b. These results provide additional evidence that the CdS layer effectively reduces defects and improves the overall solar cell performance.

The diode ideality factor (n), which offers critical information about the major recombination mechanisms in quantum dot solar cells, was determined using a logarithmic fit to the dependency of V_{oc} on light intensity to better understand the significance of the CdS passivation layer in controlling trap-assisted charge recombination. The diode ideality factor can be determined by applying a logarithmic fit to the dependence of open-circuit voltage (V_{oc}) on light intensity, using eq 4.[34] An ideal diode has an ideality factor of 1 while in practice, the presence of defects in electrodes leads to higher ideality factors ($n > 1$), as defects act as recombination centers. From the open-circuit voltage (V_{oc}) dependence on light intensity results shown in Figure 7a, the calculated ideality factors for $TiO_2/AgBiS_2$, $TiO_2/(CdS(3))/AgBiS_2$, $TiO_2/AgBiS_2/(CdS(4))$, and $TiO_2/(CdS(3))/AgBiS_2/(CdS(4))$ devices are 1.92, 1.76, 1.58, and 1.38, respectively.

As expected, the device without a CdS layer shows a high ideality factor, and after introducing a CdS layer on $AgBiS_2$ ($TiO_2/AgBiS_2/(CdS(4))$), the ideality factor was decreased to 1.58, indicating its presence on $AgBiS_2$ effectively suppresses recombination due to surface defects. Interestingly and as shown earlier, the ideality factor was further decreased to 1.38 for $TiO_2/(CdS(3))/AgBiS_2/(CdS(4))$, confirming that the most effective defect passivation can be achieved after coating CdS on both TiO_2 and $AgBiS_2$ surfaces. These results confirm that the CdS layer, particularly on the $AgBiS_2$ surface, significantly reduces recombination and is close to ideal device performance.

$$V_{oc} \cong \left(\frac{nkT}{q}\right)\ln(I) \tag{4}$$

Figure 7b shows the light intensity-dependent photocurrent measurements for $TiO_2-AgBiS_2$, $TiO_2/(CdS(3))/AgBiS_2$, $TiO_2/AgBiS_2/(CdS(4))$, and $TiO_2/(CdS(3))/AgBiS_2/(CdS(4))$ electrodes. A power–law relation $J \propto I^{\alpha}$, where α is the exponent that describes the response of the photocurrent (J) to the variation of light intensity (I) provides valuable insights into the charge transport mechanisms and bimolecular recombination processes within the devices. When α is close to 1, it indicates low recombination losses and that the photocurrent is predominantly regulated by photogenerated charge carriers. The α values obtained for $TiO_2-AgBiS_2$, $TiO_2/(CdS(3))/AgBiS_2$, $TiO_2/AgBiS_2/(CdS(4))$, and $TiO_2/(CdS(3))/AgBiS_2/(CdS(4))$ electrodes were 0.7099, 0.8231, 0.8622, and 0.9276, respectively. These results suggest that without CdS passivation, the highest deviation from the ideal value of 1, indicating more recombination. In contrast, the observed α of 0.9276 in the presence of CdS layers on both TiO_2 and $AgBiS_2$, clearly can be attributed to the decrease in bimolecular recombination leading to reduced nonradiative recombination and enhanced charge separation and transport.

To analyze the recombination behavior of $TiO_2-AgBiS_2$, $TiO_2/(CdS(3))/AgBiS_2$, $TiO_2/AgBiS_2/(CdS(4))$, and $TiO_2/(CdS(3))/AgBiS_2/(CdS(4))$ electrodes, the Tafel plots are shown in Figure 8 and the observed ideality factors under dark

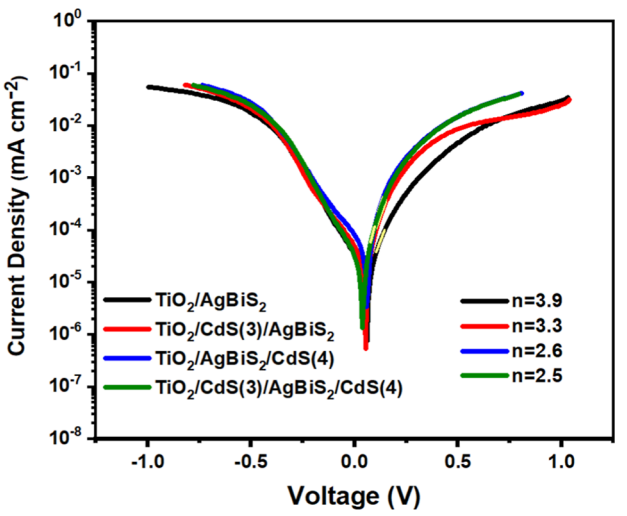

Figure 8. Dark current density vs voltage curves for the $TiO_2/AgBiS_2$, $TiO_2/(CdS(3))/AgBiS_2$, $TiO_2/AgBiS_2/(CdS(4))$, and $TiO_2/CdS(3)/AgBiS_2/CdS(4)$. The corresponding ideality factors (n) are also shown in the Figure.

conditions were 3.9, 3.3, 2.6, and 2.5, respectively. The ideality factor calculated from Tafel plots provides vital insights into the kinetic parameters and recombination mechanisms, with values greater than one indicating the presence of multiple recombination mechanisms within the device. Higher ideality factors suggest that $AgBiS_2$ has intrinsic charge recombination properties due to the presence of a large number of defect states, which can be partially reduced by passivating the CdS layer. Higher ideality factors for $AgBiS_2$ nanocrystals, on the other hand, indicate that charge recombination is a major

https://doi.org/10.1021/acsaem.5c01968
ACS Appl. Energy Mater. XXXX, XXX, XXX−XXX

deceptive element that must be addressed in order to increase the solar cell efficiency.

These results underscore the function of CdS in boosting charge collection and overall solar cell performance, with placing CdS on $AgBiS_2$ significantly lowering recombination losses. As illustrated schematically in Figure 9, the presence of

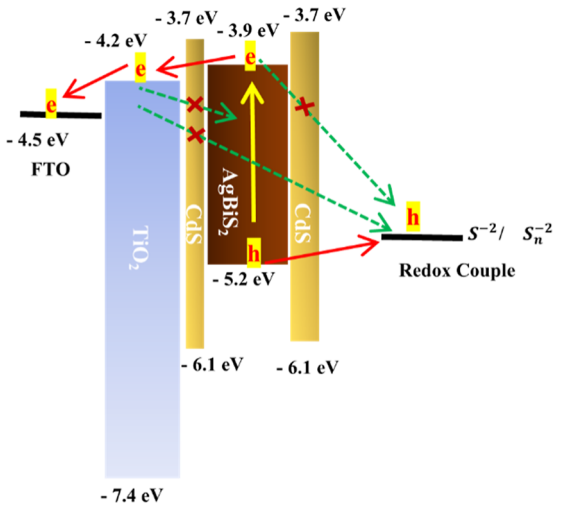

Figure 9. Schematic illustrations of charge-transfer and carrier recombination processes of the FTO/TiO_2/CdS(3)/$AgBiS_2$/CdS-(4)/electrolyte.

a CdS layer effectively reduces charge recombination steps such as recombination at the $AgBiS_2$/electrolyte and TiO_2/electrolyte interfaces, as well as the suppression of recombination of trapped charge carriers in TiO_2 with trapped holes in $AgBiS_2$ Q-dots, resulting in an overall improvement in solar cell performance. As the prime objective of this investigation was mainly focused on improving the photophysical properties and device efficiency of $AgBiS_2$ solar cells using CdS passivation, no testing was conducted on continuous illumination or environmental stress illumination stability testing. The long-term stability of the device is one of the critical factors in the practical use of photovoltaic technologies; further investigation into the long-term operational stability and degradation mechanisms of CdS-coated $AgBiS_2$ solar cells is necessary and will be considered in future studies.

Although this study focuses on CdS as the passivation layer, earlier work using ZnS under similar conditions resulted in a lower device efficiency of approximately 1.1%. The enhanced performance with CdS (PCE ~ 2.46%) is likely due to more favorable band alignment, improved interfacial contact, and more effective carrier transport. These results support the choice of CdS in the present study. However, further comparison to other inorganic passivation layers, such as MgO, could provide additional insights in future investigations.

Table S3 compares key device performance characteristics such as PCE, J_{sc}, V_{oc}, and FF from our work with other representative state-of-the-art $AgBiS_2$ Q-dot solar cells described in the literature. The observed PCE of 2.46% for the liquid electrolyte-based solar cell is a substantial improvement over the reported similar $AgBiS_2$ Q-dot solar cells, but it remains below the theoretical limit. The passivation mechanism used in this system for liquid-based electrolytes can be easily applied to solid-state electrolytes (e.g., P3HT or Spiro-OMeTAD). Furthermore, improving interfacial band alignment, advanced conformal growth of passivation layers to reduce trap states, and enhancing the nanocrystal film quality to increase carrier diffusion lengths are still viable options. Incorporating light-trapping structures or different buffer layers to increase both the absorption and charge collection efficiency could further help. Exploring these approaches in future research will optimize the performance of the device. It is also important to iterate that the usage of cadmium-based compounds has known toxicity and disposal challenges that must be addressed when considering practical photovoltaic applications. In this study, CdS was employed as a passivation layer to improve the interface properties of $AgBiS_2$ nanocrystals. While the quantity of cadmium used is low in relation to the other technologies, such as CdTe, it is nevertheless significant enough to raise concerns. This emphasizes the importance of safe handling, device encapsulation, and end-of-life recycling, especially for large-scale manufacturing and commercialization. Furthermore, these findings provide insights for the design of $AgBiS_2$-based devices with solid hole transport layers, highlighting opportunities for improved interface engineering and suggesting future studies to optimize device performance and stability.

4. CONCLUSION

The solar cell efficiency of $AgBiS_2$-based light harvesting material is shown to suffer from charge recombination losses due to the presence of a large number of inherent defect states in $AgBiS_2$ nanocrystals. Charge recombination across the $AgBiS_2$-electrolyte interface is the dominant recombination loss mechanism, and the greater ideality factor for $AgBiS_2$ nanocrystals suggests that charge recombination is a major deceptive element that must be addressed in order to improve solar cell efficiency. The coating of a CdS layer to $AgBiS_2$ particles effectively reduces charge recombination steps at the $AgBiS_2$/electrolyte and TiO_2/electrolyte interfaces, as well as recombination of trapped charge carriers in TiO_2 with trapped holes in $AgBiS_2$ Q-dots, resulting in an overall improvement in solar cell performance. As a result, the SILAR process for fabricating CdS and AgBiS2 layers is scalable and low-temperature, making it appropriate for large-area deposition. Nonetheless, using a liquid electrolyte in the current device architecture has issues with long-term stability and scalability. Future research will focus on replacing liquid electrolytes with solid-state or gel-based alternatives to improve device integration and operational stability.

■ ASSOCIATED CONTENT

Supporting Information

The Supporting Information is available free of charge at https://pubs.acs.org/doi/10.1021/acsaem.5c01968.

XRD images, SEM images, EDS images, UV−vis spectra, EQE spectra J−V curves, and XPS images (PDF)

■ AUTHOR INFORMATION

Corresponding Author

Jayasundera Bandara − *National Institute of Fundamental Studies, Kandy 20000 Central Province, Sri Lanka;*
orcid.org/0000-0001-8530-5679;
Email: jayasundera.ba@nifs.ac.lk

https://doi.org/10.1021/acsaem.5c01968
ACS Appl. Energy Mater. XXXX, XXX, XXX−XXX

Authors

Dimuthumal Rajakaruna − *National Institute of Fundamental Studies, Kandy 20000 Central Province, Sri Lanka*

Hong-yi Tan − *Guangzhou Institute of Energy Conversion, Chinese Academic of Sciences, Guangzhou 510640, China*

Chang-Feng Yan − *Guangzhou Institute of Energy Conversion, Chinese Academic of Sciences, Guangzhou 510640, China;* orcid.org/0000-0001-7096-1761

Complete contact information is available at: https://pubs.acs.org/10.1021/acsaem.5c01968

Author Contributions

The manuscript was written through the contributions of all authors. The experimental part was mainly carried out by D. Rajakaruna and characterization was supported by H. Tan.

Notes

The authors declare no competing financial interest.

■ ACKNOWLEDGMENTS

The authors are grateful for the Natural Science Foundation of China (52276222), the Guangdong Basic and Applied Basic Research Foundation of Guangdong (2024A1515010042), and the International Partnership Program of the Chinese Academy of Sciences (118GJHZ2022029MI).

■ REFERENCES

(1) Nykyruy, L. I.; Yavorskyi, R. S.; Zapukhlyak, Z. R.; Wisz, G.; Potera, P. Evaluation of CdS/CdTe thin film solar cells: SCAPS thickness simulation and analysis of optical properties. *Opt. Mater.* **2019**, *92*, 319−329.

(2) Keller, J.; Kiselman, K.; Donzel-Gargand, O.; Martin, N.; Babucci, M.; Lundberg, O.; Wallin, E.; Stolt, L.; Edoff, M. High-concentration silver alloying and steep back-contact gallium grading enabling copper indium gallium selenide solar cell with 23.6% efficiency. *Nat. Energy* **2024**, *9*, 467−478.

(3) Chalapathi, U.; Sangaraju, S.; Kumar, Y. B. K.; Cheruku, R.; Kondaiah, P.; Lavanya, M.; Gonuguntla, V.; Alhammadi, S.; Albaqami, M. D.; Sheikh, M.; Park, S.-H. Synthesis of AgBiS2 films by sulfurizing Bi/Ag stacks for thin film photovoltaics. *Opt. Mater.* **2024**, *152*, 115492.

(4) Park, J. Y.; Park, G.; Bae, S. Y.; Kim, H. J.; Lee, D. H.; Ko, S.; Kim, S.-K.; Lee, G.; You, H. R.; Choi, H.; et al. Ecofriendly AgBiS2 Nanocrystal Photoanode for Highly Efficient Visible-Light-Driven Photoelectrochemical Water Splitting. *ACS Appl. Energy Mater.* **2023**, *6* (7), 3872−3880.

(5) Ming, S.; Liu, X.; Zhang, W.; Xie, Q.; Wu, Y.; Chen, L.; Wang, H.-Q. Eco-friendly and stable silver bismuth disulphide quantum dot solar cells via methyl acetate purification and modified ligand exchange. *J. Cleaner Prod.* **2020**, *246*, 118966.

(6) Zou, B.; Chen, D.; Qammar, M.; Ding, P.; Ko, P. K.; Wu, W.; Shivarudraiah, S. B.; Yan, H.; Halpert, J. E. In Situ Surface Metal Passivation on AgBiS2 Nanocrystals for Trap-Reduced Inverted Solar Cells. *ACS Appl. Energy Mater.* **2024**, *7* (19), 8271−8277.

(7) Adeyemi, A. N.; Clemente, M.; Lee, S. J.; Mantravadi, A.; Zaikina, J. V. Deep Eutectic Solvent-Assisted Microwave Synthesis of Thermoelectric AgBiS2 and Cu3BiS3. *ACS Appl. Energy Mater.* **2022**, *5* (12), 14858−14868.

(8) Burgués-Ceballos, I.; Wang, Y.; Akgul, M. Z.; Konstantatos, G. Colloidal AgBiS2 nanocrystals with reduced recombination yield 6.4% power conversion efficiency in solution-processed solar cells. *Nano Energy* **2020**, *75*, 104961.

(9) Senina, A.; Prudnikau, A.; Wrzesińska-Lashkova, A.; Vaynzof, Y.; Paulus, F. Cation exchange synthesis of AgBiS 2 quantum dots for highly efficient solar cells. *Nanoscale* **2024**, *16* (19), 9325−9334.

(10) Burgués-Ceballos, I.; Wang, Y.; Konstantatos, G. Mixed AgBiS 2 nanocrystals for photovoltaics and photodetectors. *Nanoscale* **2022**, *14* (13), 4987−4993.

(11) Oh, J. T.; Cho, H.; Bae, S. Y.; Lim, S. J.; Kang, J.; Jung, I. H.; Choi, H.; Kim, Y. Improved size distribution of AgBiS2 colloidal nanocrystals by optimized synthetic route enhances photovoltaic performance. *Int. J. Energy Res.* **2020**, *44* (13), 11006−11014.

(12) Cojocaru, L.; Jena, A. K.; Yamamiya, M.; Numata, Y.; Ikegami, M.; Miyasaka, T. Solution-Crystalized AgBiS2 Films for Solar Cells Generating a Photo-Current Density Over 31 mA cm− 2. *Advanced Science* **2024**, *11* (44), 2406998.

(13) Wang, Y.; Kavanagh, S. R.; Burgués-Ceballos, I.; Walsh, A.; Scanlon, D. O.; Konstantatos, G. Cation disorder engineering yields AgBiS2 nanocrystals with enhanced optical absorption for efficient ultrathin solar cells. *Nat. Photonics* **2022**, *16* (3), 235−241.

(14) Li, X.; Yu, H.; Ma, X.; Liu, Z.; Huang, J.; Shen, Y.; Wang, M. Thin film AgBiS2 solar cells with over 10% power conversion efficiency enabled by vapor-assisted solution process treatment. *Chem. Eng. J.* **2024**, *495*, 153328.

(15) Tang, F.; Yao, X.; Ying, C.; Xu, L.; Shi, C. J. C. L. The preparation of AgBiS2 sensitized TiO2 nanorod array solar cells and photovoltaic performance of the corresponding solar cells. *Chem. Lett.* **2022**, *51* (5), 577−580.

(16) Liang, N.; Chen, W.; Dai, F.; Wu, X.; Zhang, W.; Li, Z.; Shen, J.; Huang, S.; He, Q.; Zai, J. J. C.; et al. Homogenously hexagonal prismatic AgBiS 2 nanocrystals: controlled synthesis and application in quantum dot-sensitized solar cells. *CrystEngComm* **2015**, *17* (9), 1902−1905.

(17) Calva-Yáñez, J.; Pérez-Valdovinos, O.; Reynoso-Soto, E.; Alvarado-Tenorio, G.; Jaramillo-Quintero, O.; Rincón, M. Interfacial evolution of AgBiS2 absorber layer obtained by SILAR method in hybrid solar cells. *J. Phys. D: Appl. Phys.* **2019**, *52* (12), 125502.

(18) Huang, P.-C.; Yang, W.-C.; Lee, M.-W. AgBiS2 Semiconductor-Sensitized Solar Cells. *J. Phys. Chem. C* **2013**, *117* (36), 18308−18314.

(19) Mehdaoui, L.; Miloua, R.; Khadraoui, M.; Bensaid, M. O.; Abdelkader, D.; Chiker, F.; Bouzidi, A. Theoretical analysis of electronic, optical, photovoltaic and thermoelectric properties of AgBiS2. *Phys. B* **2019**, *564*, 114−124.

(20) Sayeem, S. A.; Siddika, M. A.; Basu, S. R.; Mondal, B. K.; Hossain, J. Numerical Expedition on the Potential of AgBiS2-Based Thin Film Solar Cells Employing Different Carrier Transport Layers. *ACS Omega* **2024**, *9* (33), 35490−35502.

(21) Akhil, S.; Balakrishna, R. G. AgBiS2 as a photoabsorber for eco-friendly solar cells: a review. *J. Mater. Chem. A* **2022**, *10* (16), 8615−8625.

(22) Xiao, Y.; Wang, H.; Awai, F.; Shibayama, N.; Kubo, T.; Segawa, H. Eco-friendly AgBiS2 nanocrystal/ZnO nanowire heterojunction solar cells with enhanced carrier collection efficiency. *ACS Appl. Mater. Interfaces* **2021**, *13* (3), 3969−3978.

(23) Yang, W.; Sun, T.; Ma, X.; Yu, H.; Shi, H.; Hu, Y.; Huang, J.; Liu, Z.; Xu, Y.; Li, X.; et al. Boosting Open-Circuit Voltage of AgBiS2 Quantum Dot Solar Cells through Post-treatment Passivation. *ACS Energy Lett.* **2025**, *10* (1), 58−67.

(24) Diedenhofen, S. L.; Bernechea, M.; Felter, K. M.; Grozema, F. C.; Siebbeles, L. D. Charge Photogeneration and Transport in AgBiS 2 Nanocrystal Films for Photovoltaics. *Sol. RRL* **2019**, *3* (8), 1900075.

(25) Liu, Z.; Li, X.; Ma, X.; Yu, H.; Yang, W.; Luo, R.; Liu, Y.; Shen, Y.; Wang, M. Preparation of AgBiS2 thin films with vapor-assisted solution method for flexible near-infrared photodetectors. *Next Energy* **2025**, *7*, 100235.

(26) Zhong, Q.; Zhao, B.; Ji, Y.; Li, Q.; Yang, X.; Chu, M.; Hu, Y.; Li, L.; Li, S.; Xu, H.; et al. Solvent-Engineering-Assisted Ligand Exchange Strategy for High-Efficiency AgBiS2 Quantum Dot Solar Cells. *Angew. Chem., Int. Ed.* **2024**, *63* (52), No. e202412590.

(27) Burgués-Ceballos, I.; Wang, Y.; Konstantatos, G. Mixed AgBiS2 nanocrystals for photovoltaics and photodetectors. *Nanoscale* **2022**, *14* (13), 4987−4993.

(28) Treber, F.; De Grande, E.; Cappel, U. B.; Johansson, E. M. J. Effect of different halide-based ligands on the passivation and charge carrier dynamics in AgBiS2 nanocrystal solar cells. *J. Mater. Chem. A* **2024**, *12* (45), 31432−31444.
(29) Manjceevan, A.; Bandara, J. Robust surface passivation of trap sites in PbS q-dots by controlling the thickness of CdS layers in PbS/CdS quantum dot solar cells. *Sol. Energy Mater. Sol. Cells* **2016**, *147*, 157−163.
(30) Manjceevan, A.; Bandara, J. Systematic stacking of PbS/CdS/CdSe multi-layered quantum dots for the enhancement of solar cell efficiency by harvesting wide solar spectrum. *Electrochim. Acta* **2018**, *271*, 567−575.
(31) Mawaddah, F. A. N.; Bisri, S. Z. Advancing Silver Bismuth Sulfide Quantum Dots for Practical Solar Cell Applications. *Nanomaterials* **2024**, *14* (16), 1328.
(32) Bae, S. Y.; Yang, J.; Oh, J. T.; Lee, C. B.; Song, H.; Lee, B. R.; Jin, H. M.; Kim, K.; Hong, J. P.; Kim, Y.; et al. Understanding the cation-selective ligand passivation for AgBiS2 nanocrystal photovoltaics. *Chem. Eng. J.* **2023**, *474*, 145674.
(33) Tennakone, K.; Bandara, J.; Bandaranayake, P. K. M.; Kumara, G. R. A.; Konno, A. Enhanced efficiency of a dye-sensitized solar cell made from MgO-coated nanocrystalline SnO2. *Jpn. J. Appl. Phys.* **2001**, *40* (7B), L732.
(34) Rajakaruna, D.; Tan, H.-y.; Yan, C.-F.; Bandara, J. Assessment of interface passivation in AgBiS2 Q-dot sensitized solar cell on the carrier transport and recombination. *Electrochim. Acta* **2025**, *526*, 146173.
(35) Akhil, S.; Kusuma, J.; Balakrishna, R. G. Green AgBiSe2/AgBiS2 core shell quantum dots for stable solar cells by robust SILAR method. *J. Cleaner Prod.* **2022**, *366*, 132760.
(36) Calva-Yáñez, J. C.; Pérez-Valdovinos, O.; Reynoso-Soto, E. A.; Alvarado-Tenorio, G.; Jaramillo-Quintero, O.; Rincón, M. Interfacial evolution of AgBiS 2 absorber layer obtained by SILAR method in hybrid solar cells. *J. Phys. D: Appl. Phys.* **2019**, *52*, 125502.
(37) Wijerathna, C. N.; Tan, H.-y.; Yan, C.-F.; Bandara, J. Improving light harvesting and charge carrier separation enabling enhanced photoelectrochemical hydrogen production by Sb2S3-decorated TiO2 nanotube arrays on porous Ti-photoanodes. *Int. J. Hydrogen Energy* **2024**, *82*, 53−63.
(38) Katoch, M.; Pal, N. Prediction of Optical Transmittance Loss In Solar Panels Using Lambert-Beer Law. In *2019 3rd International Conference on Recent Developments in Control, Automation & Power Engineering (RDCAPE), 10−11 Oct. 2019*, 2019, pp 357−361..
(39) Di Capua, R.; Offi, F.; Fontana, F. Check the Lambert-Beer-Bouguer law: A simple trick to boost the confidence of students toward both exponential laws and the discrete approach to experimental physics. *Eur. J. Phys.* **2014**, *35*, 045025.
(40) Diedenhofen, S.; Bernechea, M.; Felter, K.; Grozema, F. C.; Siebbeles, L. Charge Photogeneration and Transport in AgBiS2 Nanocrystal Films for Photovoltaics. *Sol. RRL* **2019**, *3* (8), 1900075.
(41) Zhang, Y.; Wu, G.; Mora-Seró, I.; Ding, C.; Liu, F.; Huang, Q.; Ogomi, Y.; Hayase, S.; Toyoda, T.; Wang, R.; et al. Improvement of Photovoltaic Performance of Colloidal Quantum Dot Solar Cells Using Organic Small Molecule as Hole-Selective Layer. *J. Phys. Chem. Lett.* **2017**, *8* (10), 2163−2169.
(42) Li, W.; Pan, Z.; Zhong, X. CuInSe2 and CuInSe2-ZnS based High Efficiency "Green" Quantum Dot Sensitized Solar Cells. *J. Mater. Chem. A* **2015**, *3*, 1649.
(43) Jung, S. W.; Kim, J.-H.; Kim, H.; Choi, C.-J.; Ahn, K.-S. ZnS overlayer on *in situ* chemical bath deposited CdS quantum dot-assembled TiO_2 films for quantum dot-sensitized solar cells. *Curr. Appl. Phys.* **2012**, *12* (6), 1459−1464.
(44) Gupta, G.; Garg, A.; Dixit, A. Electrical and impedance spectroscopy analysis of sol-gel derived spin coated Cu 2 ZnSnS 4 solar cell. *J. Appl. Phys.* **2018**, *123*, 013101.
(45) Mahan, J. E.; Ekstedt, T. W.; Frank, R. I.; Kaplow, R. Measurement of minority carrier lifetime in solar cells from photo-induced open-circuit voltage decay. *IEEE Trans. Electron Devices* **1979**, *26* (5), 733−739.
(46) Chang, J.; Kuga, Y.; Mora-Seró, I.; Toyoda, T.; Ogomi, Y.; Hayase, S.; Bisquert, J.; Shen, Q. High Reduction of Interfacial Charge Recombination in Colloidal Quantum Dot Solar Cells by Metal Oxide Surface Passivation. *Nanoscale* **2015**, *7* (12), 5446−5456.
(47) Zhang, Y.; Ding, C.; Wu, G.; Nakazawa, N.; Chang, J.; Ogomi, Y.; Toyoda, T.; Hayase, S.; Katayama, K.; Shen, Q. Air Stable PbSe Colloidal Quantum Dot Heterojunction Solar Cells: Ligand-Dependent Exciton Dissociation, Recombination, Photovoltaic Property, and Stability. *J. Phys. Chem. C* **2016**, *120* (50), 28509−28518.

https://doi.org/10.1021/acsaem.5c01968
ACS Appl. Energy Mater. XXXX, XXX, XXX−XXX